

Directional detection of dark matter with diamond

Mason C. Marshall^{1,2}, Matthew J. Turner^{3,4}, Mark J.H. Ku^{3,5,6},
David F. Phillips², Ronald L. Walsworth^{1,2,6,7}

¹ Department of Electrical and Computer Engineering, University of Maryland, College Park, Maryland, 20742, USA

² Center for Astrophysics | Harvard & Smithsonian, Cambridge, Massachusetts, 02138, USA

³ Department of Physics, Harvard University, Cambridge, Massachusetts, 02138, USA

⁴ Center for Brain Science, Harvard University, Cambridge, MA, 02138, USA

⁵ Department of Physics and Astronomy, University of Delaware, Newark, DE, 19716, USA

⁶ Quantum Technology Center, University of Maryland, College Park, Maryland, 20742, USA

⁷ Department of Physics, University of Maryland, College Park, Maryland, 20742, USA

September 2020

Abstract. Searches for WIMP dark matter will in the near future be sensitive to solar neutrinos. Directional detection offers a method to reject solar neutrinos and improve WIMP searches, but reaching that sensitivity with existing directional detectors poses challenges. We propose a combined atomic/particle physics approach using a large-volume diamond detector. WIMP candidate events trigger a particle detector, after which spectroscopy of nitrogen vacancy centers reads out the direction of the incoming particle. We discuss the current state of technologies required to realize directional detection in diamond and present a path towards a detector with sensitivity below the neutrino floor.

1. Introduction

Weakly interacting massive particles (WIMPs) remain one of the most compelling dark matter (DM) models after decades of searches [1]. WIMPs are a dark matter candidate which, via thermal freeze-out, arise in an abundance consistent with the observed dark matter density. Additionally, WIMP candidates arise naturally in many beyond-standard-model theories [2]. Direct detection of WIMPs is a long-term and ongoing effort, with exclusion bounds on cross-sections and WIMP masses shrinking by several orders of magnitude each over the past three decades [3].

Upcoming detectors are expected to reach sensitivity levels allowing detection of solar neutrinos [4, 5]. Coherent elastic neutrino scattering events induce single nuclear recoils [6], and therefore pass cuts looking for electron recoils or multiple scattering due

to backgrounds such as cosmic rays and radioisotope contamination of target materials and instrumentation. Solar neutrinos thus constitute an irreducible background for future WIMP detectors – the “neutrino floor.” Discovering a dark matter particle will therefore require identifying annual modulation of a WIMP signal as the Earth’s velocity changes relative to a putative WIMP “wind” [7]. To do so on top of a large solar neutrino background will demand dozens of DM events.

An alternative approach to extend WIMP searches below the neutrino floor is directional detection [8, 9]. If the direction of an incoming particle can be determined, solar neutrino events can be discriminated, allowing a low-background search for cosmological dark matter particles. A number of routes are being pursued towards directional DM detection using a variety of target materials, each with its own advantages and disadvantages. Gas-phase detectors [10, 11, 12, 13, 14] have well-developed directional discrimination; but because the sensitivity of a DM detector depends on its total mass, gas-phase detectors will require extremely large volumes to reach the sensitivity of liquid- or solid-phase detectors. Emulsion-phase detectors [15, 16] have higher target density than gaseous detectors, but require lengthy readout times post-exposure, and only allow time-integrated directional detection. Directional scintillators [17] reach solid-state target density and use traditional particle physics readout techniques, but do not give directional information for individual events — the measured energy for each event is shifted depending on the incoming particle’s direction, requiring day-night variation (and thus many events) to extract a directional signal. Dual-phase liquid noble gas detectors may be extended to partial directional discrimination by taking advantage of columnar recombination [18], but extensive development is still required.

We envision a “hybrid” approach whereby directional detection can be incorporated into a more traditional WIMP detector, with a solid-state target mass and using well-developed instrumentation and background-discrimination methods [19]. Such a hybrid detector would identify WIMP candidate events using traditional methods like charge, phonon, or scintillation collection. In our hybrid technique, we extend semiconductor detection technologies to include directional detection — specifically, in a detector with diamond as its target material. Diamond is the subject of active study for next-generation semiconductor-based WIMP detectors — it offers excellent semiconductor properties, and the relatively light carbon nucleus provides an improved sensitivity profile for low-mass DM candidates [20] compared to xenon or other heavy target materials. We will not provide a detailed discussion of traditional event detection in diamond here, but we note that this is an active topic of research, with ongoing investigations around the world [20, 21].

To achieve sensitivity below the neutrino floor, a large total target mass will be required — comparable to the multi-ton masses of other next-generation WIMP detectors, with diamond volumes at the cubic meter scale. Modern diamond growth techniques using chemical vapor deposition (CVD) enable repeatable, fast growth of uniform crystals, and with realistic development should be capable of producing the

volumes of diamond necessary for such a detector. Optimized crystal growth protocols [22] lead to both advantageous semiconductor properties, allowing for very sensitive charge and phonon extraction, and also very uniform, low crystal strain. When a WIMP scatters in the diamond crystal, it is expected to impart substantial kinetic energy to a single carbon nucleus, which initiates multiple secondary recoils. In addition to producing charge carrier, phonon, and photon emission, these recoils will leave lattice vacancies, interstitial nuclei, and distorted bonds, combining to cause strain in the form a damage track originating at the site of the WIMP interaction. For recoil energies above ~ 3 keV, these damage tracks are predicted to exhibit measurable head-tail asymmetry, and to be oriented near the direction of the incoming particle [19]. The basic principle of directional detection in diamond is thus as follows: first, a WIMP candidate event in a segmented diamond target triggers traditional particle-detection systems. The relevant segment is then removed from the bulk of the detector; the crystal damage from the WIMP is measured and the direction read out. Together with the detector position at the time of the event, the damage track's direction gives the WIMP incident direction relative to the sun and the galactic halo.

For recoils with energy in the range 10–100 keV, corresponding to WIMP masses in the 1–100 GeV range, damage tracks will be tens of nanometers long. After localizing a WIMP candidate event to a single CVD diamond chip [23], of order 1 mm^3 , within the cubic meter bulk of the detector, key technical challenges remain to extracting the direction of the incoming particle. Scanning the entire chip with resolution below 10 nm would be time-prohibitive, and wide-field techniques are diffraction-limited by the wavelength of the applied laser light ($\sim 0.5\text{ }\mu\text{m}$). We therefore propose a three-step process for a diamond directional detector, illustrated in Fig. 1:

- First, an event is registered and triangulated on the mm scale by photon, phonon, or charge-carrier collection.
- Second, using diffraction-limited optics the event's damage track is localized to a $\sim\mu\text{m}$ voxel within the diamond.
- Finally, superresolution optical methods or high-resolution x-rays map the damage track at the nanoscale, yielding the required directional information.

In the following sections, we describe our initial work on track localization and super-resolution imaging to determine the direction from which a WIMP or neutrino arrives at a DM detector.

2. Recoil localization with strain mapping by NV spectroscopy

The great advantage of a diamond detector, beyond its sensitivity to low-mass WIMP candidates, is the existence of well-characterized, photoactive quantum defects. Using quantum defects as integrated sensors for local crystal damage is the key enabling technology for a directional DM detector in diamond. Specifically, the nitrogen vacancy

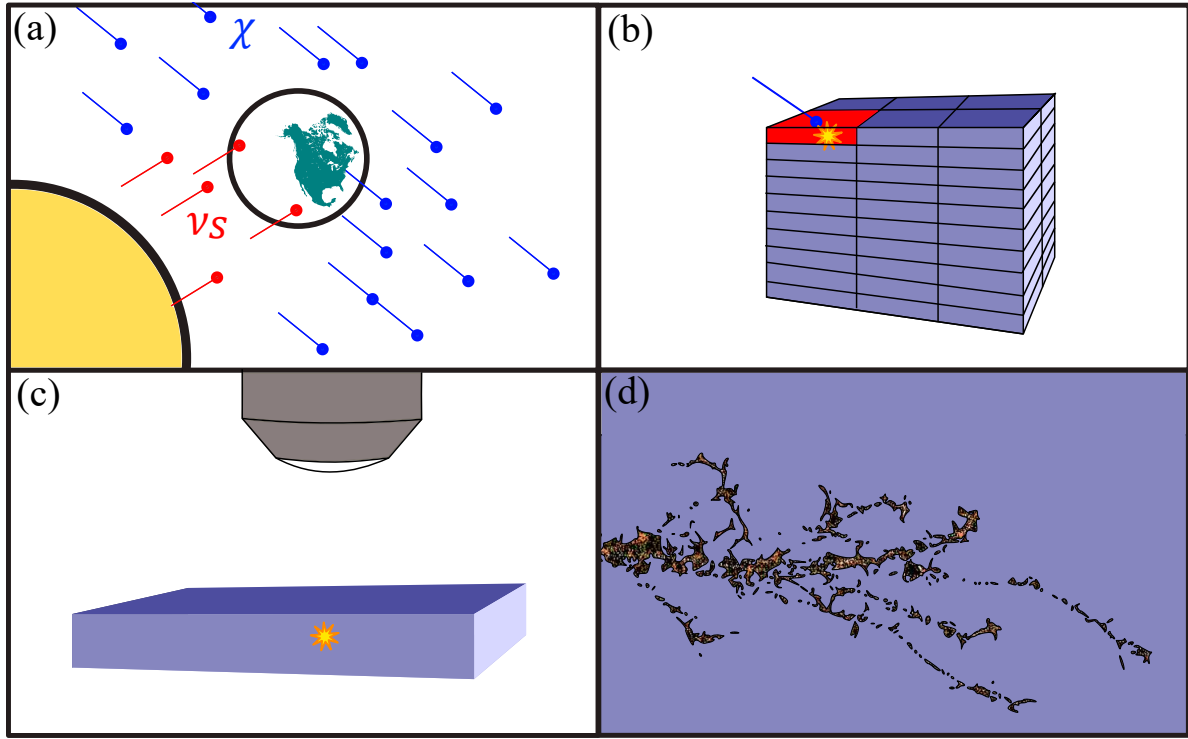


Figure 1. Schematic overview of the proposed dark matter detection procedure. (a) The Earth passes through the galactic WIMP (χ) distribution (WIMP ‘wind’) as solar neutrinos (ν_s) arrive from the Sun. An underground detector is carried by the rotation of the Earth and interacts with the incoming neutrinos and WIMPs. (b) Occasionally, a WIMP or neutrino initiates a nuclear recoil cascade via collision with a carbon nucleus in the detector, depositing energy and damaging the crystal lattice; the event is detected by charge, photon, or phonon collection. The time of the event is recorded, giving the orientation of the detector relative to the Sun and galactic WIMP wind. (c) The triggered segment is removed from the detector bulk; using diffraction-limited optical methods, the nuclear recoil track is localized to a $\sim \mu\text{m}^3$ volume. (d) Finally, the distribution of crystal damage in the nuclear recoil track is measured and reveals the incoming direction of the particle, allowing statistical discrimination of WIMPs and neutrinos.

(NV) center has been extensively characterized and used for a wide variety of quantum sensing applications [24, 25, 26, 27]. In this section, we evaluate the use of NV centers to accomplish the mm-to- μm scale localization step for directional detection.

The NV center is a fluorescent point defect consisting of a substitutional nitrogen impurity adjacent to a lattice site vacancy, illustrated in Fig. 2a. The defect features an electron in a spin-1 ground state with a microwave transition frequency which is sensitive to magnetic and electric fields, as well as local crystal strain. The spin state can be optically initialized, and read out via the spin-dependent red fluorescence emitted after excitation with green light. Via their strain sensitivity, NV centers act as integrated sensors for nearby crystal damage [28], presenting methods for both diffraction-limited and superresolution detection of nuclear recoil tracks.

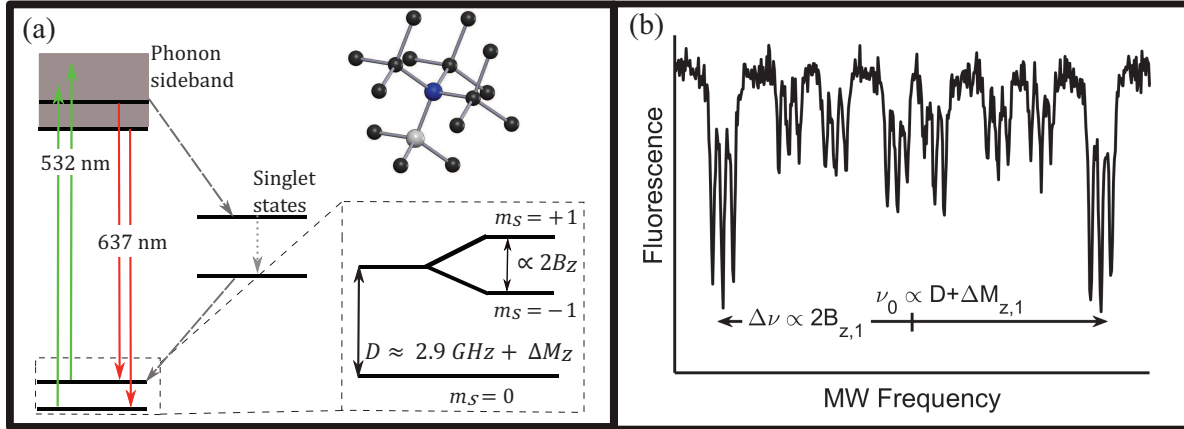


Figure 2. (a) Negatively charged NV center energy level structure ($S=1$). Electronic energy level transitions are excited into vibrational continuum states with green light and emit red light. The $m_s = \pm 1$ spin level exhibits reduced red fluorescence due to the presence of an alternate, non-radiative decay path. Microwave spectroscopy enables strain and magnetic field measurements. (See text.) Inset: NV diamond crystal structure. Here, carbon atoms of the diamond lattice are shown in black; the gray ball represents a vacancy in the lattice structure while the blue represents a nitrogen atom replacing one of the carbon atoms. (b) Example NV spectrum with an applied bias magnetic field. Four pairs of hyperfine triplet resonances are produced by the four NV directions in an ensemble aligned with the crystal axes; each resonance has a center frequency ν_0 which depends on temperature and local strain, as well as a frequency splitting $\Delta\nu$ between the $m_s = 0$ to $m_s = \pm 1$ states proportional to the magnetic field component along the NV axis, $B_{z,i}$ where $i = 1, 2, 3, 4$.

Here, we consider the use of NV sensing to detect crystal strain features — local deformations in the diamond crystal lattice. Strain — a relative change in the lattice spacing from its equilibrium value — occurs in CVD diamond both due to imperfections which propagate during growth and flaws in surface processing [29]. Strain features in diamond have been studied using a variety of methods, including birefringence imaging [30], x-ray tomography [31], and Raman imaging [32]. Because of its deleterious effect on NV center-based magnetic field measurements [33], strain has been studied extensively in this regard [28, 34]. While intrinsic strain is a contaminant to observing damage tracks left by particle scattering, the same methods used to study intrinsic strain can be used to pinpoint the position of WIMP-induced damage tracks.

2.1. State of the art in NV strain imaging

NV strain imaging measurements are typically performed using a “quantum diamond microscope” (QDM) [35], as illustrated in Fig. 3. An NV-rich diamond is illuminated with green laser light, and the spin-dependent red fluorescence is collected by a microscope objective and imaged with a camera. The NV spin is addressed by microwaves, and the transition frequencies determined by resonant reduction in the fluorescence (Fig. 2b). Magnetic fields split the transition frequencies, while changes in

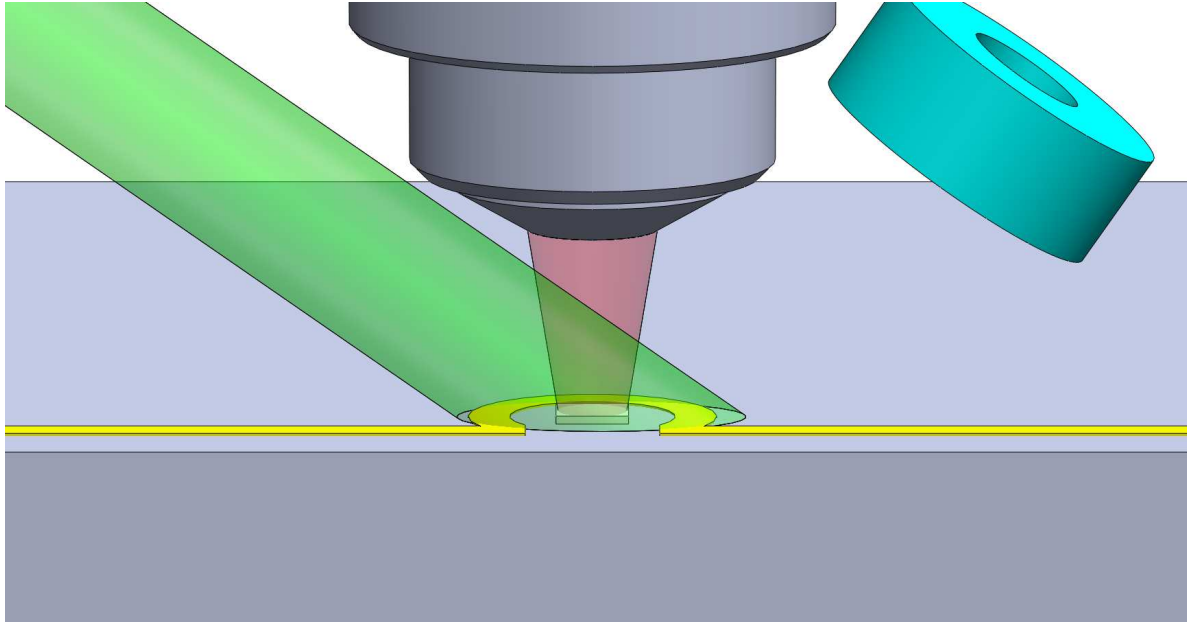


Figure 3. Simplified schematic of a quantum diamond microscope (QDM), as used for wide-field strain imaging with nitrogen vacancy (NV) centers. An NV-bearing diamond is illuminated by green laser light; NV centers emit red fluorescence, which is collected by a microscope objective and focused onto a camera (not shown). The ground-state spin transition is probed by microwaves emitted by a waveguide (gold). A bias field is provided by permanent magnets (teal) and/or Helmholtz coils (also not shown).

strain and temperature yield common-mode shifts as shown in Fig. 2. Diamond is an excellent thermal conductor, and temperature thus can be assumed to be homogeneous across the diamond; spatially resolved measurements of common-mode frequency shifts are therefore maps of relative crystal strain. This method has been used to study strain at boundaries in polycrystalline diamond [36]; strain induced by implanted ions [34]; and strain due to growth defects in CVD diamond layers [28]. The strain sensitivity achievable with such measurements depends on the particular properties of the diamond samples used, such as density and coherence time of the NV centers used, as well as experimental factors such as camera sensitivity and resolution and instrumentation noise. To evaluate the suitability of QDM strain measurement for damage track localization, we compare in Table 1 the results reported in previous strain-imaging experiments. We also extrapolate strain sensitivity from the reported sensitivity of some magnetic QDM experiments.

2.2. Estimate of WIMP-induced strain signal in QDM

Following [39] and [19], we assume a fractional strain from a WIMP scattering event in diamond of approximately $\frac{\Delta x}{x} \sim 10^{-6}$ at a distance of 30 nm from a single vacancy, leading to an NV resonance shift of about 30 kHz. As strain falls off as $1/r^3$, the strain

Table 1. Sample strain imaging measurements from the literature for diamonds with various nitrogen vacancy (NV) densities and layer thicknesses.

Sample type	Strain noise floor	Reported noise floor	Lateral resolution	Averaging time	Ref.
Ensemble doped	2E-7	1 kHz	4 μm	3 hours	[28]
Thin implant	1E-6	1 MPa	1 μm	10 hours	[34]
Single NVs	4E-6	4E-6	<1 μm	120 seconds	[36]
Ensemble doped	1E-7*	20 nT	5 μm	11 hours	[37]
Thin implant	5E-7*	100 nT	<1 μm	(not listed)	[38]

*Extrapolated strain sensitivity for magnetic-field imaging experiments

from an entire damage cluster can be found by adding the strain from each individual point defect. To determine the average signal, we find the strain shift for NV centers at each point within an imaging voxel, yielding the lineshape a QDM would see at that voxel. We treat the damage track as a cylinder with height and radius 30 nm, and assume the strain within that cylinder induces a uniform 10^{-6} shift; this avoids complications in calculating the specific distribution of damage within the region. Outside the cylinder, we calculate the strain using a $1/r^3$ scaling with distance from the cylinder.

An NV center is most sensitive to the projection of strain onto the axis between the nitrogen and the vacancy [28]. Depending on the orientation of the crystal damage and its position within a voxel, the projection of strains onto different NV centers could add constructively, or average to zero. We therefore extract two quantities from our estimate — a mean of strain magnitudes, representing the case in which strain adds across the voxel; and a standard deviation, based on a distribution of strains with a mean of zero. Figure 4 shows the distribution of strains within two different micron-thick voxels — one with a diffraction-limited, 350 nm spot, and the other with a volume of $1 \mu\text{m}^3$. These distributions are computed for a damage track from a 10 keV scattering event, yielding approximately 50 vacancies; the strain amplitudes for higher-energy events will increase accordingly. Note that the horizontal scale is limited to $\pm 2 \times 10^{-6}$ — while NV centers near the damage track will experience strains up to $\sim 50 \times 10^{-6}$, most NV centers in the voxel will have lower strains. The mean strain magnitudes and linewidths can be extracted from the distributions in two ways - including or excluding these high-strain NVs. The appropriate comparison will depend on experimental details, including (for example) the efficiency of the camera used in the QDM and its ability to detect light from a few, high-strain NVs, or the spin coherence properties of NVs in the diamond material. Table 2 gives estimated voxel-averaged, WIMP-induced strain for different measurement parameters. These results vary by approximately one order of magnitude between 1×10^{-7} and 3×10^{-6} .

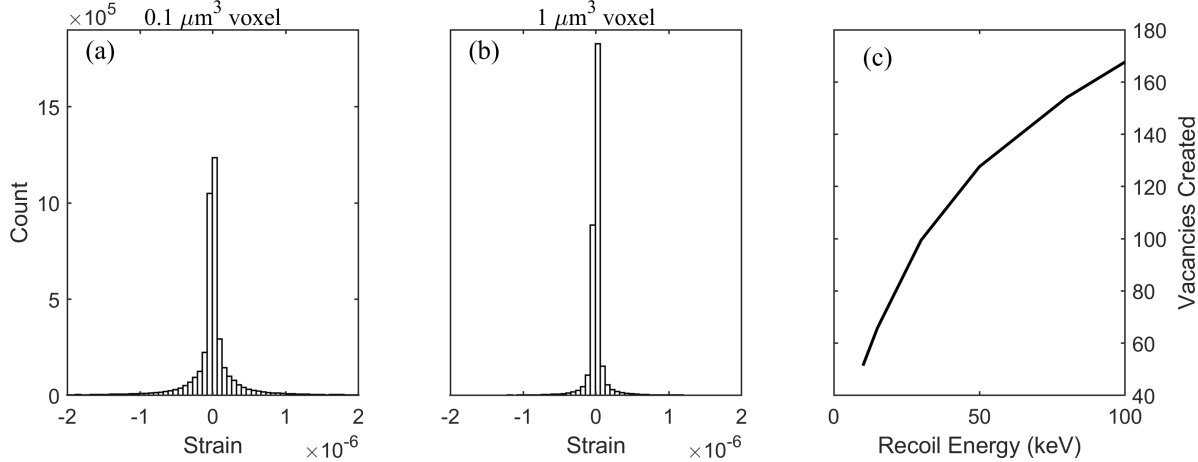


Figure 4. (a) Distribution of diamond strain within a laterally diffraction-limited voxel of axial depth $1 \mu\text{m}$ and volume $\sim 0.1 \mu\text{m}^3$, containing a nuclear recoil track from 10 keV of deposited energy in a WIMP collision. Calculational details are described in the text. (b) As (a) but for a $1 \mu\text{m}^3$ voxel. (c) Number of vacancies created for different initial recoil energies, calculated using the SRIM simulation software [40].

Table 2. Estimated strain signal amplitudes.

Signal type	Voxel size	High-strain NVs	Voxel-averaged strain
Mean shift	Diffraction-limited	Included	7×10^{-7}
Mean shift	Diffraction-limited	Excluded	3×10^{-7}
Mean shift	$1 \mu\text{m}^3$	Included	2×10^{-7}
Mean shift	$1 \mu\text{m}^3$	Excluded	1×10^{-7}
St. Dev.	Diffraction-limited	Included	3×10^{-6}
St. Dev.	Diffraction-limited	Excluded	6×10^{-7}
St. Dev.	$1 \mu\text{m}^3$	Included	2×10^{-6}
St. Dev.	$1 \mu\text{m}^3$	Excluded	3×10^{-7}

2.3. Improving strain spectroscopy

While the ~ 100 ppb (parts per billion) noise floor of the best QDM measurements [35, 37] is sensitive enough to detect the signal from a damage track, two technical barriers remain to WIMP track localization via strain spectroscopy. First, these techniques simultaneously collect fluorescence from the entire depth of the NV-bearing diamond layer, whereas to localize a damage track we must restrict the vertical position to a $\sim 1 \mu\text{m}$ spot, likely by restricting the optical point spread function (PSF) or using applied magnetic field gradients to select a specific region of NVs via Zeeman shifts of NV spin levels [41]. Second, the multi-hour averaging times required to resolve small strains are prohibitive, requiring hundreds of days to image $1000 \mu\text{m}$ -thick slices in a single detector segment. After a segment is removed from the bulk of the detector, it will be

exposed to higher rates of background radiation; while this can be reduced by performing optical measurements on-site at the shielded complex housing the detector, radiation from non-ultralow-background materials in (for example) the QDM structure and optics may create damage. Measurement times of order 1 day are therefore preferred. The reported spatial resolution for the most sensitive previous measurements compiled in Table 1 is also worse than the requisite ~ 1 micron; however, this resolution is limited by collection of light in a thick NV layer, so restricting the axial PSF would improve lateral resolution as well.

Advanced techniques from NV magnetic imaging offer a path to sufficiently fast measurement times. All of the strain and magnetic field measurements in Table 1 are performed using continuous-wave (CW) microwave excitation of the NV spins. Measurement protocols using pulsed microwaves take advantage of the NV's quantum coherence to dramatically improve data collection speed. For example, wide-field magnetic field imaging measurements using a pulsed protocol have recently been reported, achieving a noise floor comparable to the most sensitive CW QDM measurements with a few seconds of averaging time [42]. This protocol requires homogeneous microwave power across the imaged area, and thus suffers from a reduced field of view compared to the CW QDM; however, this limitation is more than compensated by measurement speed, and a pulsed imager would reduce search times by more than two orders of magnitude. Unlike the CW QDM experiments in Table 1, the magnetic sensitivity reported in [42] is not directly analogous to strain sensitivity – the measurement protocol used is, in fact, insensitive to crystal strain. Pulsed-microwave protocols, constructed to be sensitive to strain and temperature variations and unaffected by magnetic field gradients, have been used for sensitive NV thermometry [43, 44, 45], and their implementation in a wide-field imaging configuration could resolve averaging time issues for WIMP track detection. This promising direction will be pursued in future work.

The other outstanding challenge to NV strain spectroscopy is restricting the sensed region in z , or depth into the diamond. Even high numerical aperture optics with small depth of field collect out-of-focus light, reducing sensitivity to small strains. A number of optical sectioning methods commonly used in biological imaging could be adapted to imaging with NV centers. In particular, structured illumination microscopy (SIM) takes advantage of the increased attenuation away from the focal plane of light modulated with high spatial frequency to reject out-of-focus, unmodulated light [46] and has been implemented to achieve superresolution imaging in diamond [47]. Light-sheet microscopy uses a cylindrical lens to create a thin sheet of laser light, restricting the excitation volume [48]; this technique has also been implemented in diamond to measure the properties of microwave devices [49]. Implementation in diamond of these techniques will enable μm localization of nuclear recoil tracks - SIM has so far only been used in diamond to achieve lateral superresolution with a quasi-two-dimensional distribution of NV centers, while the thinnest light sheet in [49] was $14\ \mu\text{m}$. Nevertheless, given extensive development of these techniques in the biosciences, achieving a cubic

μm voxel is a realistic target.

An alternative technique, scanning confocal laser microscopy, inherently rejects out-of-focus light. The confocal excitation and detection spot can be scanned through the sample volume, giving three-dimensional information (as shown in Fig. 6 below). A strain-sensitive pulse sequence, together with high laser power density and sensitive detection, would enable fast measurement at each point; however, measuring $\sim 10^9$ voxels of $1 \mu\text{m}^3$ volume is challenging. To scan a diamond in one day, each point would need to be measured in under $100 \mu\text{s}$; improved wide-field strain spectroscopy therefore presents a more realistic approach.

2.4. Strain in CVD diamond

Measuring small strains quickly is only one component of detecting the signature from WIMP recoil tracks. Additionally, the host diamond must exhibit sufficiently low strain to make such measurements possible. Large-scale strain gradients hurt sensitivity by shifting the NV center spin resonance away from the microwave drive frequency. The edges of strain features can exhibit high-spatial-frequency strain variation, leading to unmeasurable pixels and possibly masking damage tracks [28]. Additionally, intrinsic strain features with lengths of a micron or less could appear to be damage tracks themselves, yielding false positives. All CVD diamond is grown by deposition of diamond crystal layers on a pre-existing substrate, and recent advances in processing of these substrates — as well as other growth techniques — allow creation of NV-rich bulk diamond with low strain inhomogeneity over millimeter length scales [22], suppressing both large gradients and high-gradient pixels. Figure 5 shows QDM strain maps of NV-rich CVD diamonds, grown using recently developed low-strain techniques. Wide-area gradients are suppressed below 1 MHz across the field of view, and all NV centers can be addressed by a typical MW pulse. Aside from a few large features arising from defects at the CVD-substrate interface, individual strain features have amplitudes below the level of all but the weakest DM signals.

In addition to being a good host for wide-field NV strain spectroscopy, a suitable diamond detector segment cannot have intrinsic strain features that mimic damage tracks. Pre-exposure scanning of the entire large-volume ($\sim \text{m}^3$) detector would be prohibitive — such features must either be forbidden by the growth process or removed by post-processing of the detector material. There are two types of strain features at relevant length scales for false positives — larger than point defects, but smaller than a micron: crystal growth defects such as dislocations and twinning, and extended vacancy clusters [29, 50]. Crystal growth defects propagate upwards from the substrate during growth, and can be suppressed by careful surface processing [29] and choice of diamond growth parameters. Additionally, the propagation of crystal defects during diamond growth renders them easily distinguishable from recoil tracks if the $1 \mu\text{m}$ slice for imaging is chosen to be perpendicular to the growth direction [31], or by combining axial slices to measure the three-dimensional shape of the feature, as in Fig. 6b. Meanwhile, vacancy

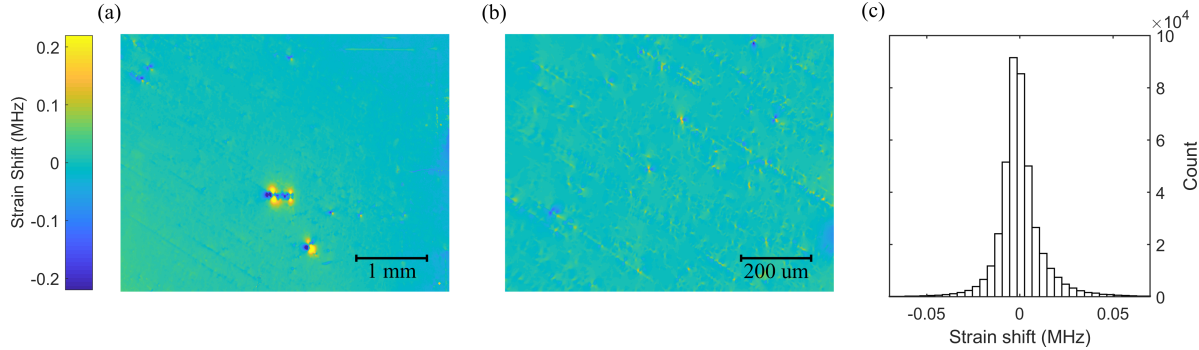


Figure 5. Quantum diamond microscope (QDM) strain images of a 40 μm -thick, NV-rich diamond layer grown on an electronic-grade single-crystal diamond substrate. **(a)** Wide-field QDM image reveals minimal strain at the millimeter scale across the sample, allowing strain-sensitive measurements without retuning or parameter changes. Also visible are several spatially large, high-strain features propagating from imperfections at the substrate surface. **(b)** Increasing the magnification and subtracting the linear gradient observed in (a) reveals smaller, weaker strain features. **(c)** A histogram of residual strain per pixel in (b). The standard deviation of 0.014 MHz is comparable to the projected range of WIMP-induced strain amplitudes of 0.003–0.090 MHz (Table 2). The few pixels with strain at or over the projected signal amplitude can be differentiated from a real signal by spatial shape size; further development in diamond growth will continue to narrow the strain distribution in NV-rich diamond layers.

clusters are found to break up during high-temperature annealing [22], keeping strain low; high-resolution x-ray diffraction measurements show no evidence of strain-inducing features with length scales between 20 and 100 nm [51], indicating that they either are not produced during deposition or are broken up during annealing. Confocal scanning strain measurements have also not found evidence of micron-scale strain features in bulk NV-rich diamond (Fig. 6a). We note that these measurements were performed over limited sample volumes, and only show that these features are not widespread — before operation of a prototype detector, a more thorough background search will be necessary.

2.5. Cryogenic zero phonon line NV spectroscopy

In addition to shifting the microwave transition frequency of the NV electron's spin, local strain also shifts the optical transition frequency of the NV orbital energy level [52]. This frequency shift could be used to identify high-strain pixels in a damage track search. Doing so requires spectroscopy on the zero phonon line (ZPL) - the electronic energy level transition without absorption or emission of an accompanying phonon. At room temperature the ZPL is too broad to measure small strain shifts — for temperatures below 100 K its linewidth increases proportionally to T^5 because of the dynamic Jahn-Teller effect [53]. At cryogenic temperatures, however, such strain shifts have been used to precisely locate NVs within a diffraction-limited spot: positions of nearby NV centers were resolved to 1 nm using a tunable laser [54]. For wide-field track localization, the

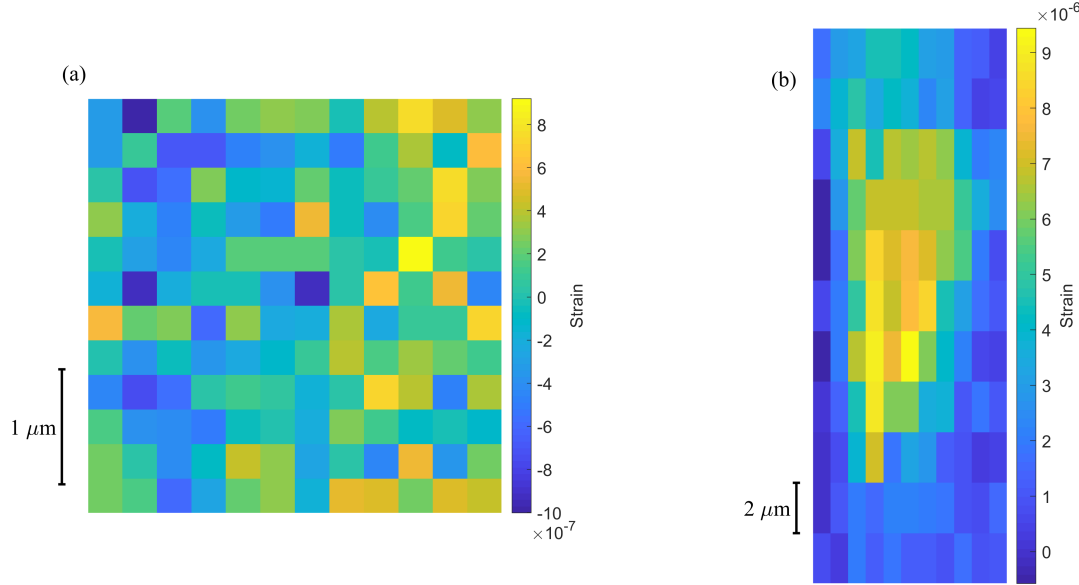


Figure 6. Scanning confocal microscope NV strain maps. (a) High-resolution, narrow-field survey of a 500 μm -thick, NV-enriched bulk diamond. Standard deviation of strain per pixel of 4×10^{-7} approaches levels needed for WIMP-induced damage track detection. (b) Axial slice of a small strain feature in the same diamond featured in Fig. 5. Growth defect strain features can be distinguished from damage tracks by their axial extent.

detector segment under investigation could be held at cryogenic temperatures, and the ZPL interrogated with such a tunable laser. NV centers under sufficient local strain will fluoresce at a distinct excitation wavelength from their neighbors; those near a WIMP-induced damage track should experience strains greater than 10^{-6} , corresponding to shifts in the ZPL of order 1 GHz. This is much larger than the lifetime-limited transition linewidth at cryogenic temperatures, which has been measured as low as 10 MHz [55]; also, measuring GHz shifts in optical frequency would require only modest laser stabilization. The key challenge for this technique will be collecting the fluorescence from single or few NV centers near the damage track using widefield laser excitation and image acquisition; however, this is achievable using EM-CCD cameras [56, 36]. Measurement times for the ZPL and QDM methods should be comparable, as each requires sweeping an excitation frequency and measuring a number of slices along the z-axis. However, each technique has distinct signal-to-noise challenges. The feasibility of the ZPL method depends on the averaging time required to detect single or few NV centers; the QDM method depends on our ability to exclude background fluorescence from out-of-focus NV centers and achieve optimal strain resolution using pulsed MW sequences. The optimal balance for each method remains to be experimentally investigated.

3. Damage track localization with NV center creation

The crystal damage in a WIMP candidate damage track is expected to consist of dozens to hundreds of recoil-induced lattice site vacancies. Vacancies in diamond become mobile under high-temperature annealing, and may combine with a nearby nitrogen impurity to form an NV center [57, 58]. In a diamond with high nitrogen content, recoil-induced vacancies could be annealed to produce NV centers at the site of a WIMP event. If the high-nitrogen diamond also had few initial NVs, this would enable a nearly background-free localization via the fluorescence of the induced NV centers.

Fluorescence microscopy on radiation-induced defects as a method for nuclear recoil detection is a mature technique, largely using $\text{Al}_2\text{O}_3:\text{C},\text{Mg}$ crystals referred to as “fluorescent nuclear track detectors” (FNTDs) [59]. These provide an instructive case study for track localization via induced fluorescence. Color centers — $\text{F}_2^{2+}(2\text{Mg})$ — are formed in $\text{Al}_2\text{O}_3:\text{C},\text{Mg}$ during crystal growth. Nuclear recoils induce local electron cascades, transforming the color centers via electron capture to $\text{F}_2^+(2\text{Mg})$ centers, which exhibit a distinct absorption and emission spectrum. Confocal microscopy combined with reconstructive algorithms yield 3D reconstruction of the nuclear trajectory [60], which has been applied to radiation oncology/dosimetry [61, 62], as well as nuclear [63], neutron [64], and beam [65] physics.

FNTD crystal studies have focused either on energy ranges well above 10–100 keV, or long tracks generated via irradiation with neutrons. In both cases, tracks are typically much longer than the optical diffraction length, and can be measured using confocal microscopy. Superresolution methods such as STED [66] and SIM [67] have been applied in some cases, but the best reported resolution is large compared to the length scale of an expected WIMP damage track.

A similar principle has been applied in diamond — recoil tracks are mapped via creation of NV centers using radiation-induced vacancies [68]. After exposure to high-energy ions, the diamond is annealed at high temperature, allowing the vacancies to migrate. Vacancies that migrate near pre-existing nitrogen impurities are captured, forming NV centers; these are detected via confocal fluorescence microscopy. Unlike the FNTD crystals, this process requires high-temperature annealing to “develop” the nuclear recoil tracks — recoil-induced damage in diamond is then used to study vacancy diffusion during annealing [69]. However, a key difference between FNTD crystals and diamonds is the much lower fluorescence per unit of deposited energy in diamond, due to low conversion yield of vacancies to NV centers.

Previous fluorescent track detection research in diamond has used long damage tracks from high-energy particles — higher by a factor of 10^4 than relevant energies for WIMP detection [68, 69]. With many fewer than 10^4 NVs created per ion track, this method would be unable to detect a WIMP-induced recoil. However, a modified version of this protocol using a high-nitrogen diamond could increase sensitivity to a level capable of WIMP track detection. Type Ib diamonds, grown via the high-temperature, high-pressure (HPHT) process, feature nitrogen impurities at hundreds of parts per

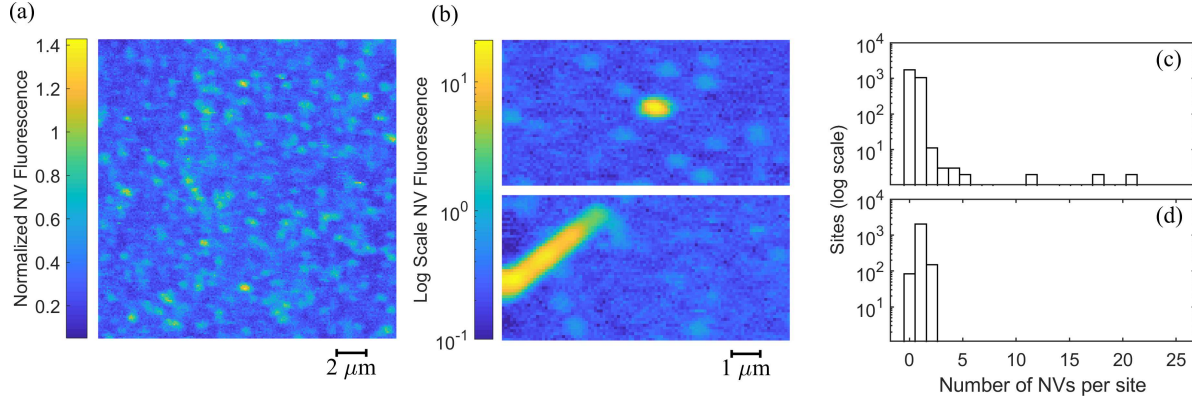


Figure 7. Confocal fluorescence collection on an annealed, high-[N], low-[NV] diamond suitable for fluorescent nuclear track detector (FNTD) studies. **(a)** Typical $10 \times 10 \mu\text{m}^2$ field of view demonstrating the pre-existing single-NV background. **(b)** The annealed diamond surface (two sections shown) includes occasional sites with higher fluorescence than a single NV center, attributable to imperfect surface polishing (or, possibly, NV conversion during past annealing cycles using vacancies created by historical background radiation exposure). **(c)** NV center positions were counted by identification of local maxima in confocal fluorescence scans. The intensity of fluorescence at each site was then used to determine the number of NVs in a diffraction-limited spot. Scans across the diamond surface reveal rare but non-negligible sites with multiple NV centers. **(d)** A similar scan taken 5-6 μm below the diamond surface revealed no pre-existing spots with more than 2 NVs per confocal limited volume, indicating that these multi-NV clusters result only from polishing imperfections and surface contamination.

million, together with very few vacancies or pre-existing NV centers [70, 71]. Initial studies, as shown in Fig. 7, find that while there are features near the surface that could be construed as false positives, no such features are found in the bulk of the diamond, indicating they are not inherent to the growth process and could be eliminated with advanced surface treatment [22]. As long as a WIMP event induces 3 or more NV centers upon annealing, this would represent an essentially background-free method to locate the WIMP event. The low background would enable either fast confocal scanning or wide-field fluorescence collection with an efficient, low-noise camera such as an EM-CCD.

To estimate whether low-energy WIMP collisions will lead to a detectable number of vacancies and resultant NVs, we perform simulations of recoil cascades using the TRIM software package [40]. In these simulations, a 10 keV recoil induces several dozen vacancies extending over approximately 20 nm. The migration range of these vacancies during annealing depends on the temperature and duration of annealing. To preserve head-tail asymmetry [19], the annealing parameters chosen must allow much less than 20 nm mean vacancy travel distance. Assuming, for our estimate, a 3 nm vacancy migration length and a typical nitrogen impurity concentration of 200 ppm for a type Ib HPHT diamond, there will be ~ 20 N nuclei available within the vacancy travel

range for NV center formation during annealing. The actual number of NVs created is difficult to predict, as it will depend not only on the number of vacancies and nitrogen nuclei available, but also on recombination rates with interstitial carbon and formation of vacancy clusters [57, 72, 73]. Because of the low background, only a few NVs need be created to locate a damage track. A detailed experimental measurement of the NV yield as a function of energy and annealing parameters is necessary to demonstrate feasibility of this technique. If track location via induced fluorescence proves viable, the high nitrogen concentration will complicate nanoscale track mapping via superresolution spectroscopy (see section 4) by reducing the NV center coherence and dephasing times [74, 75]. If the vacancy-to-NV conversion rate is high, the track direction may be determined by resolving the positions of the individual induced NVs; with lower yields, non-NV-based methods may be required, such as the X-ray spectroscopy described in section 4.2.

4. Nanoscale track direction mapping

Once the position of a WIMP (or neutrino) induced damage track has been determined to within a micron-scale voxel, the incident direction of the initial particle must be extracted from the spatial distribution of crystal damage. Damage tracks exhibit head-tail asymmetry and orientation correlated with the direction of the WIMP candidate [19]. In this section, we will discuss methods to map this crystal damage at the nanoscale. Extracting the direction from a track as short as 20–50 nm (for 10–30 keV initial recoil energy) requires a three-dimensional measurement with resolution below the track length.

4.1. Superresolution NV strain spectroscopy

Rapid developments in NV-based magnetic field sensing with spatial resolution below the optical diffraction limit have been motivated by the pursuit of nanoscale MRI [24, 76, 77]. As with wide-field magnetic imaging, techniques developed for subdiffraction magnetic sensing with NV centers can be adapted to sense crystal strain with a change of microwave pulse sequence. For WIMP track mapping, a superresolution technique must be capable of three-dimensional operation with ~ 20 nm resolution, and simultaneously allow microwave spectroscopy of the NV spin. Broadly, three classes of superresolution techniques have been applied to NV centers: deactivation techniques involving a doughnut-hole laser beam, stochastic techniques for separating individual NV centers, and techniques based on strong magnetic field gradients. We will review each of these and discuss applications to directional WIMP detection.

Several deactivation techniques have been used to localize individual NV centers separated by less than the diffraction limit or perform superresolution spectroscopy. In each case, the signal from NV centers in a doughnut-shaped laser beam spot is suppressed, allowing information to be collected only from the NVs at the small central

intensity minimum of the doughnut beam. Stimulated emission depletion, or STED, uses a strong pulsed doughnut beam to induce stimulated emission from the addressed NVs, depleting their fluorescence before data is collected. In diamonds with a thin layer of NV centers or in nanodiamonds, STED has been used for NV center localization to ~ 5 nm [78] and magnetic spectroscopy with spatial resolution < 10 nm [79, 80]. Charge state depletion (CSD) replaces the strong depletion beam with a doughnut beam at a wavelength chosen to photoionize NV^- centers to NV^0 ; in combination with optical filtering blocking NV^0 fluorescence, this allows interrogation only of the remaining NV^- at the doughnut beam's central minimum. CSD microscopy has been demonstrated to localize nearby NV centers with 4 nm resolution [81], and to perform magnetic superresolution magnetic spectroscopy in a thin, dense layer of NV centers with 45 nm spatial resolution [82]. Finally, spin-RESOLFT imaging uses a doughnut beam after a magnetic sensing microwave pulse sequence, destroying sensing information stored in NV centers under the doughnut beam and allowing spectroscopy only on NV centers in the central minimum [83]. Using shallow NV centers, this enabled magnetic spectroscopy with 20 nm spatial resolution [84].

Past demonstrations of these techniques have used either quasi-two-dimensional ensembles or relatively sparse single NV centers, which do not overlap in the axial direction. To measure a damage track, which could be anywhere in the diamond segment, requires three-dimensional resolution. A number of methods for generation of three-dimensional doughnut-hole beams in diamond have been explored; using a mirror and optical interference [85] or patterned light [86] yield ~ 100 nm resolution in the axial dimension. In biological media, two crossed doughnut beams have been used to perform STED microscopy with 45 nm resolution in all three dimensions [87], although applying this technique in diamond is complicated by the high index of refraction. Therefore, we expect these techniques to be very challenging to perform in three dimensions at the sub 20 nm resolution required to infer damage track direction.

Stochastic superresolution imaging methods, such as STORM and PALM, are widely used in biosciences and have been demonstrated using NV centers, achieving 12 nm localization [88] and magnetic sensing with 20 nm spatial resolution [89]. While high NV densities [84] impede stochastic localization of individual emitters, these techniques may prove useful in HPHT diamonds coupled with vacancy creation by damage tracks described in section 3.

An alternative method for superresolution spectroscopy uses magnetic gradients to obtain spatial localization from the NV spin precession frequency rather than the optical transition. Large magnetic gradients can be applied so that only a small class of NV centers resonate with a uniformly applied microwave control sequence, allowing spatially selective imaging with high resolution using magnetic gradient coils [90] or magnetic write heads [91]. Microfabricated gradient coils enabled magnetic spectroscopy on selectively addressed NV centers with 30 nm resolution [41]. Magnetic field gradients can also be used for position encoding, rather than position-selective addressing. In Fourier magnetic imaging, the gradient encodes an NV's position onto its spin precession phase

and frequency; post-processing the acquired images enables subdiffraction imaging. This method has been used for magnetic field imaging with a two-dimensional set of single NVs with 30 nm spatial resolution [92]. A similar method using microwave field inhomogeneity as a localization tool was demonstrated for 2D magnetic imaging with 100 nm spatial resolution in a dense NV ensemble [93].

2D spatial resolution at or near the 20 nm level has been demonstrated with all of the superresolution methods described above. This benchmark is required for determining damage track directionality. These methods are also compatible with strain-sensitive microwave interrogation. The major outstanding challenge with any of these techniques will be to employ them in a dense, three-dimensional ensemble of NV centers. With the exception of recent charge state depletion [82] and microwave-inhomogeneity assisted localization [93], demonstrations of superresolution NV spectroscopy have typically been performed in relatively low density samples, with only a few NV centers per diffraction-limited volume; a conservative estimate of the NV density required for track mapping is several hundred in such a volume [19]. Meanwhile, 3D superresolution NV imaging has only been demonstrated with STED, and only with 100 nm resolution [85, 86] (although similar techniques could be used for CSD or spin-RESOLFT imaging). To extract the direction of a 10–30 keV WIMP event will require significant improvements in optics, either by improved spatial light modulation or by successful application of crossed-beam STED in a diamond sample. Fourier magnetic imaging could also reach the required resolution, but generating appropriately large, structured three-dimensional gradients using fabricated microcoils remains challenging.

Given the current state of the art, a combination of methods, as illustrated in figure 8, will likely be required to measure the directionality of damage tracks. A two-dimensional STED or CSD beam could provide 20 nm resolution in the lateral plane, while a magnetic field gradient enables selective addressing or post-processing deconvolution for 20 nm axial resolution. A doughnut beam would be created using standard STED optics, and an appropriate microfabricated gradient coil would provide one-dimensional deconvolution of the axial position. Alternatively, the cryogenic ZPL spectroscopy method discussed in Sec. 2.5 has been used for nm-scale localization of nearby NV centers in a sparse sample [54], and could potentially be extended to three dimensions and denser ensembles.

Only some of these methods are applicable to the high-nitrogen, low-NV case described in section 3 above. Magnetic field noise from the dense bath of nitrogen impurity spins reduces the NV coherence time, complicating methods like spin-RESOLFT and Fourier magnetic imaging, which require precise spectroscopy or quantum state control. Conversely, the low density of pre-existing NV centers means that a damage track’s direction could be mapped simply by localizing the created NV centers, without requiring strain spectroscopy.

One further caveat is worth mentioning - the sub-diffraction experiments and superresolution benchmarks described above were all performed using NV centers at or near the surface of the diamond, whereas a WIMP candidate event can happen

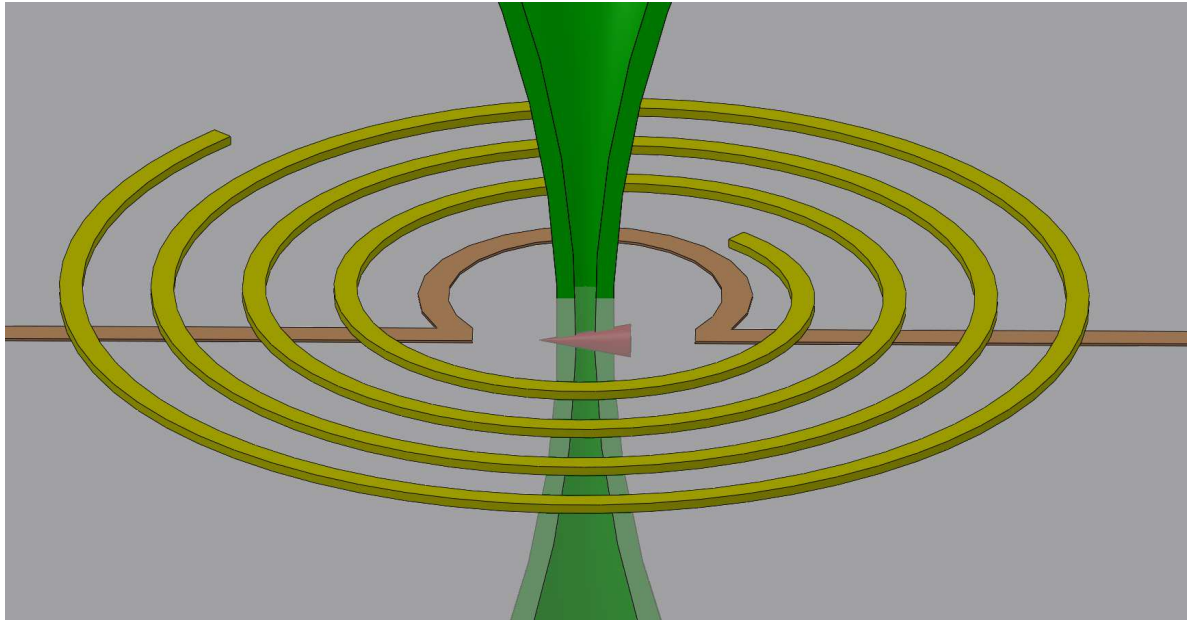


Figure 8. Proposed combined technique for three-dimensional superresolution strain spectroscopy. A doughnut optical beam, implementing either STED or CSD, enables lateral superresolution by depleting surrounding NVs. A microcoil creates a magnetic field gradient, which allows Fourier deconvolution along the vertical axis. The microcoil and microwave guide are fabricated around the micron-localized damage track position.

anywhere within the mm^3 detector section. Deeper into the diamond, the optical point spread function of any microscope is both broadened and distorted by diamond's high refractive index [94]. However, once the damage track is localized at the um^3 scale within the detector segment, diamond can be etched away until the damage track is within a few um of the nearest surface. Using appropriate techniques [29], this should be possible without introducing additional damage or strain and without distorting the WIMP signal, albeit with additional time and effort.

4.2. Nanoscale x-ray strain measurement

Strain measurements can also be made with spatial resolution below the diffraction limit for visible light by using shorter-wavelength photons. In particular, hard x-ray photons have subnanometer wavelengths and can be focused to spot sizes below 10 nm [95]. Scanning x-ray diffraction microscopy presents an alternative method for damage track localization. A variety of techniques exist for high-spatial-resolution imaging of materials structure with x-ray nanobeams, with spatial resolution of 2–50 nm and strain resolution at the 10^{-4} to 10^{-5} level [96, 97]. Hard x-ray nanobeams with appropriate resolution and sensitivity are currently found only at a few synchrotron facilities worldwide [98, 99, 100]; however, for the low expected annual event rate [19] and with accurate optical localization, the damage track direction for all candidate WIMP events could be read out with a modest amount of x-ray beam time per year.

X-ray Bragg nanodiffraction microscopy operates via a highly focused beam spot, held at a Bragg condition and scanned across a sample surface [97]; at each physical position, a segmented detector records a diffraction pattern. This diffraction pattern is sensitive to small perturbations of the crystal structure within the beam spot, allowing strain and crystal orientation to be mapped with high spatial resolution [101]. Strain measurements with spatial resolution as low as 5 nm [102] have been performed using coherent Bragg ptychography - diffraction patterns overlapping coherent beam spots can be inverted by an iterative algorithm, giving high-resolution images of the diffracting crystal structure [103]. Additionally, three-dimensional images can be retrieved by coherent Bragg ptychography, while maintaining resolution below the beam spot size [104].

While scanning nanodiffraction combines high strain and spatial resolution, a diffraction pattern at any given Bragg angle will only be sensitive to a particular subset of strain vectors - those that change the crystal lattice spacing for the plane from which the x-ray photons diffract. To fully map a damage track, it would therefore be necessary to scan the crystal from multiple Bragg angles. In addition to covering a full range of strain vectors, measuring at multiple angles would allow for three-dimensional reconstruction without ptychography; additionally, multiple-angle Bragg ptychography allows improved three-dimensional imaging, relaxing the demanding experimental constraints of single-angle Bragg ptychography [105].

Appropriate spatial resolution in three dimensions has been demonstrated with scanning x-ray diffraction microscopy. However, whether strain sensitivity is at a level necessary to detect damage tracks is uncertain. Strain resolution near 10^{-5} is routinely attainable, and strain near a WIMP-induced damage track should be above this level. The x-ray beam is focused only in two dimensions - the axial beam spot size is limited only by absorption and diffraction in the diamond, and can extend hundreds of times beyond the lateral spot size. While the shift in average strain across the entire beam spot due to a damage track may be below the detection threshold, the strained volume of diamond will diffract some of the beam to an observable angle. It should thus be possible to measure a small feature with large strain by looking for the photons diffracted from the strained subvolume rather than a shift in the average strain over the entire beam spot. This principle has been demonstrated in diamond in preliminary studies for WIMP track measurement [51]. Features with length scales close to a damage track are detectable with Bragg nanodiffraction - for example, atomic-scale variations in thickness of a 10 nm Si quantum well were measured in an Si/SiGe heterostructure [106].

As with the optical superresolution methods described above, x-ray diffraction microscopy measurements would require that, before measuring a damage track's direction, the diamond would first be etched to bring the damage track within a few microns of the surface. Additionally, as with optical measurements if performed off-site, the detector segments would need to be appropriately shielded in transit from the detector site to the synchrotron facility against cosmic rays. Notably, this method would be compatible with non-spectroscopic methods of damage track localization, including

the low-yield scenario discussed in section 3 for track detection via NV center creation.

5. Outlook and next steps

The two major technical challenges facing directional WIMP detection in diamond, damage track localization and direction measurement, have solutions requiring challenging but realistic development over existing technology. We aim, in ongoing experiments, to demonstrate the requisite improvements. Two methods for damage track localization are under development: strain spectroscopy and creation of new color centers from recoil-induced damage. One set of improvements to strain spectroscopy will adapt existing magnetic-field imaging techniques to achieve sensitive, high-spatial-resolution strain measurements; a second experiment demonstrating restriction of the excitation light with either light-sheet or structured-illumination microscopy will follow. Event localization via fluorescent nuclear track detection requires a 10^4 reduction in detected ion energy over previous experiments, but with high-nitrogen, low-fluorescence diamonds this should be possible; characterization of fluorescence creation under these conditions is underway.

Two methods for extracting the incoming particle direction via nanoscale mapping of damage tracks are also under consideration. Three-dimensional superresolution strain spectroscopy using a combination of a two-dimensional doughnut-hole beam and one-dimensional Fourier magnetic gradient deconvolution would only require combining existing technologies, while cryogenic zero phonon line spectroscopy offers a superresolution method using only Gaussian optics. Finally, synchrotron measurements with a nanofocused x-ray beam are also underway. The initial step is to demonstrate separate measurement of a small, strained subvolume in an unstrained, NV-rich diamond; next steps include injected-ion measurements to evaluate sensitivity, as well as demonstrating three-dimensional Bragg ptychography in a diamond sample.

Reaching sensitivities below the neutrino floor for WIMP dark matter searches with reasonable exposures will likely require directional detection. Diamond is a promising material for future WIMP target development. Building on over a decade of research into the NV center and the excellent crystalline and optical properties of CVD and HPHT diamond should enable directional detection in diamond with further technique development. A combined high-energy/atomic physics approach may then provide directional dark matter searches with solid-state density, opening a route to WIMP sensitivity below the neutrino floor.

6. Acknowledgements

We acknowledge technical discussions and assistance from Pauli Kehayias, Connor Hart, Raisa Trubko, Alex Sushkov, Martin Holt, Tao Zhou, F. Joseph Heremans, Nazar Delegans, and Surjeet Rajendran. This work was supported by the DOE QuANTISED program under Award No. DE-SC0019396; the Army Research Laboratory MAQP

program under Contract No. W911NF-19-2-0181; the DARPA DRINQS program under Grant No. D18AC00033; and the University of Maryland Quantum Technology Center.

7. References

- [1] Roszkowski L, Sessolo E M and Trojanowski S 2018 *Reports on Progress in Physics* **81** 066201 ISSN 0034-4885
- [2] Arcadi G, Dutra M, Ghosh P, Lindner M, Mambrini Y, Pierre M, Profumo S and Queiroz F S 2018 *The European Physical Journal C* **78** 203 ISSN 1434-6052
- [3] Schumann M 2019 *Journal of Physics G: Nuclear and Particle Physics* **46** 103003 ISSN 0954-3899
- [4] Böehm C, Cerdeño D G, Machado P A N, Campo A O D and Reid E 2019 *Journal of Cosmology and Astroparticle Physics* **2019** 043–043 ISSN 1475-7516
- [5] Ng K C, Beacom J F, Peter A H and Rott C 2017 *Physical Review D* **96** 103006
- [6] Akimov D, Albert J B, An P, Awe C, Barbeau P S, Becker B, Belov V, Brown A, Bolozdynya A, Cabrera-Palmer B, Cervantes M, Collar J I, Cooper R J, Cooper R L, Cuesta C, Dean D J, Detwiler J A, Eberhardt A, Efremenko Y, Elliott S R, Erkela E M, Fabris L, Febbraro M, Fields N E, Fox W, Fu Z, Galindo-Uribarri A, Green M P, Hai M, Heath M R, Hedges S, Hornback D, Hossbach T W, Iverson E B, Kaufman L J, Ki S, Klein S R, Khromov A, Konovalov A, Kremer M, Kumpa A, Leadbetter C, Li L, Lu W, Mann K, Markoff D M, Miller K, Moreno H, Mueller P E, Newby J, Orrell J L, Overman C T, Parno D S, Penttila S, Perumpilly G, Ray H, Raybern J, Reyna D, Rich G C, Rimal D, Rudik D, Scholberg K, Scholz B J, Sinev G, Snow W M, Sosnovtsev V, Shakirov A, Suchyta S, Suh B, Tayloe R, Thornton R T, Tolstukhin I, Vanderwerp J, Varner R L, Virtue C J, Wan Z, Yoo J, Yu C H, Zawada A, Zettlemoyer J and Zderic A M 2017 *Science* **357** 1123–1126 ISSN 0036-8075 (*Preprint* <https://science.sciencemag.org/content/357/6356/1123.full.pdf>) URL <https://science.sciencemag.org/content/357/6356/1123>
- [7] Freese K, Lisanti M and Savage C 2013 *Reviews of Modern Physics* **85** 1561–1581
- [8] O'Hare C A, Green A M, Billard J, Figueroa-Feliciano E and Strigari L E 2015 *Physical Review D* **92** 063518
- [9] Grothaus P, Fairbairn M and Monroe J 2014 *Physical Review D* **90** 055018
- [10] Miuchi K, Nishimura H, Hattori K, Higashi N, Ida C, Iwaki S, Kabuki S, Kubo H, Kurosawa S, Nakamura K, Parker J, Sawano T, Takahashi M, Tanimori T, Taniue K, Ueno K, Sekiya H, Takeda A, Tsuchiya K and Takada A 2010 *Physics Letters B* **686** 11–17 ISSN 0370-2693
- [11] Battat J, Brack J, Daw E, Dorofeev A, Ezeribe A, Gauvreau J L, Gold M, Harton J, Landers J, Law E, Lee E, Loomba D, Lumnah A, Matthews J, Miller E, Monte A, Mouton F, Murphy A, Paling S, Phan N, Robinson M, Sadler S, Scarff A, Schuckman II F, Snowden-Ifft D, Spooner N, Telfer S, Vahsen S, Walker D, Warner D and Yuriev L 2015 *Physics of the Dark Universe* **9–10** 1–7 ISSN 2212-6864
- [12] Riffard Q, Santos D, Guillaudin O, Bosson G, Bourrion O, Bouvier J, Descombes T, Fourel C, Muraz J F, Lebreton L, Maire D, Colas P, Ferrer-Ribas E, Giomataris I, Busto J, Fouchez D, Brunner J and Tao C 2017 *Journal of Instrumentation* **12** P06021–P06021 ISSN 1748-0221
- [13] Deaconu C, Leyton M, Corliss R, Druitt G, Eggleston R, Guerrero N, Henderson S, Lopez J, Monroe J and Fisher P 2017 *Physical Review D* **95** 122002
- [14] Nakamura K D, Ban S, Hirose M, Ichikawa A K, Ishiyama Y, Minamino A, Miuchi K, Nakaya T, Sekiya H, Tanaka S and Ueshima K 2018 *J. Inst.* **13**(07) P07015–P07015
- [15] Agafonova N, Aleksandrov A, Anokhina A, Asada T, Ashikhmin V, Bodnarchuk I, Buonaura A, Chernyavskii M, Chukanov A, D'Ambrosio N, De Lellis G, Di Crescenzo A, Di Marco N, Dmitrievski S, Enikeev R, Fini R, Galati G, Gentile V, Gorbunov S, Gornushkin Y, Guler A, Ichiki H, Katsuragawa T, Konovalova N, Kuge K, Lauria A, Lee K, Lista L, Malgin A, Managadze A, Monacelli P, Montesi M, Naka T, Okateva N, Park B, Podgrudkov D, Polukhina N, Pupilli F, Roganova T, Rogozhnikov A, Rosa G, Ryazhskaya O, Sato O, Shakiryanova I,

Shchedrina T, Sirignano C, Sohn J, Sotnikov A, Starkov N, Strolin P, Tioukov V, Umemoto A, Ustyuzhanin A, Yoon C, Yoshimoto M and Vasina S 2018 *The European Physical Journal C* **78** 578 ISSN 1434-6052

[16] Gorbunov S A and Konovalova N S 2020 *Physics of Atomic Nuclei* **83** 83–91 ISSN 1562-692X

[17] Belli P, Bernabei R, Cappella F, Caracciolo V, Cerulli R, Cherubini N, Danevich F, Incicchitti A, Kasperovych D, Merlo V, Piccinelli E, Polischuk O and Tretyak V 2020 *The European Physical Journal A* **56** 83 ISSN 1434-601X

[18] Cadeddu M, Lissia M, Agnes P, Batignani G, Bonivento W, Bottino B, Caravati M, Catalanotti S, Cataudella V, Cicalò C, Cocco A, Covone G, Candia A d, Filippis G, Rosa G, Davini S, Devoto A, Dionisi C, Franco D, Giganti C, Galbiati C, Giagu S, Gulino M, Kuss M, Lista L, Longo G, Navrre-Agasson A, Pallavicini M, Pandola L, Paoloni E, Picciano E, Razeti M, Rescigno M, Riffard Q, Rossi B, Rossi N, Testera G, Trinchese P, Tonazzo A, Walker S and Fiorillo G 2019 *Journal of Cosmology and Astroparticle Physics* **2019** 014–014 ISSN 1475-7516

[19] Rajendran S, Zobrist N, Sushkov A O, Walsworth R and Lukin M 2017 *Physical Review D* **96** 035009

[20] Kurinsky N, Yu T C, Hochberg Y and Cabrera B 2019 *Physical Review D* **99** 123005

[21] Canonica L, Abdelhameed A, Bauer P, Bento A, Bertoldo E, Ferreiro Iachellini N, Fuchs D, Hauff D, Mancuso M, Petricca F, Pröbst F and Rothe J 2020 *Journal of Low Temperature Physics* **199** 606–613 ISSN 1573-7357

[22] Edmonds A, Hart C, Turner M, Colard P O, Schloss J, Olsson K, Trubko R, Markham M, Rathmill A, Horne-Smith B, Lew W, Manickam A, Bruce S, Kaup P, Russo J, DiMario M, South J, Hansen J, Twitchen D and Walsworth R 2020 *arXiv:2004.01746 [cond-mat, physics:quant-ph]* ArXiv: 2004.01746 URL <http://arxiv.org/abs/2004.01746>

[23] McKinsey D N and the LZ collaboration 2016 *Journal of Physics: Conference Series* **718** 042039 ISSN 1742-6596

[24] Schirhagl R, Chang K, Loretz M and Degen C L 2014 *Annual Review of Physical Chemistry* **65** 83–105

[25] Maze J, Stanwix P, Hodges J, Hong S, Taylor J, Cappellaro P, Jiang L, Dutt M, Togan E, Zibrov A, Yacoby A, Walsworth R and Lukin M 2008 *Nature* **455** 644–647 ISSN 1476-4687

[26] Dolde F, Fedder H, Doherty M, Nöbauer T, Rempp F, Balasubramanian G, Wolf T, Reinhard F, Hollenberg L, Jelezko F and Wrachtrup J 2011 *Nature Physics* **7** 459–463 ISSN 1745-2481

[27] Pham L, Sage D, Stanwix P, Yeung T, Glenn D, Trifonov A, Cappellaro P, Hemmer P, Lukin M, Park H, Yacoby A and Walsworth R 2011 *New Journal of Physics* **13** 045021 ISSN 1367-2630

[28] Kehayias P, Turner M J, Trubko R, Schloss J M, Hart C A, Wesson M, Glenn D R and Walsworth R L 2019 *Physical Review B* **100** 174103

[29] Friel I, Clewes S L, Dhillon H K, Perkins N, Twitchen D J and Scarsbrook G A 2009 *Diamond and Related Materials* **18** 808–815 ISSN 0925-9635

[30] Hoa L T M, Ouisse T, Chaussende D, Naamoun M, Tallaire A and Achard J 2014 *Crystal Growth & Design* **14** 5761–5766 ISSN 1528-7483

[31] Gaukroger M P, Martineau P M, Crowder M J, Friel I, Williams S D and Twitchen D J 2008 *Diamond and Related Materials* **17** 262–269 ISSN 0925-9635

[32] Crisci A, Baillet F, Mermoux M, Bogdan G, Nesládek M and Haenen K 2011 *physica status solidi (a)* **208** 2038–2044 ISSN 1862-6319

[33] Barry J F, Schloss J M, Bauch E, Turner M J, Hart C A, Pham L M and Walsworth R L 2020 *Reviews of Modern Physics* **92** 015004

[34] Broadway D, Johnson B, Barson M, Lillie S, Dotschuk N, McCloskey D, Tsai A, Teraji T, Simpson D, Stacey A, McCallum J, Bradby J, Doherty M, Hollenberg L and Tetienne J P 2019 *Nano Letters* **19** 4543–4550 ISSN 1530-6984

[35] Levine E V, Turner M J, Kehayias P, Hart C A, Langellier N, Trubko R, Glenn D R, Fu R R and Walsworth R L 2019 *Nanophotonics* **8** 1945–1973

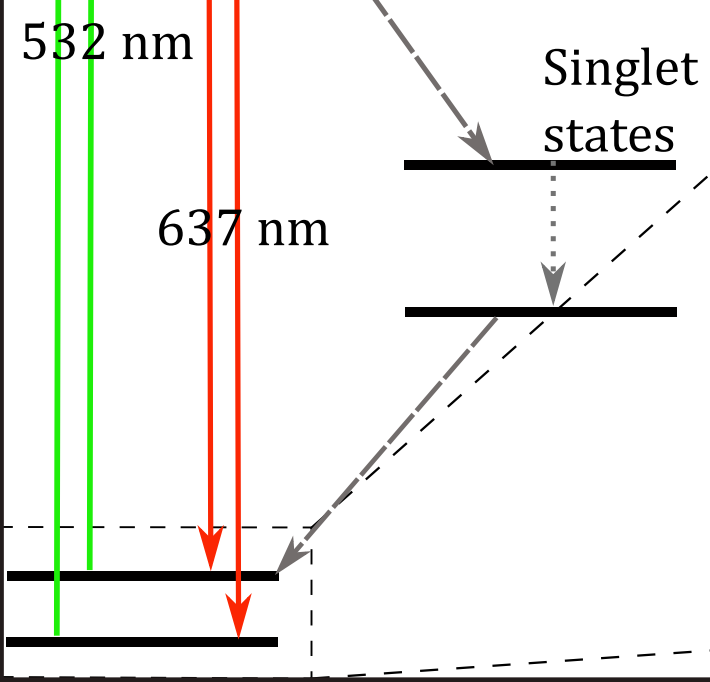
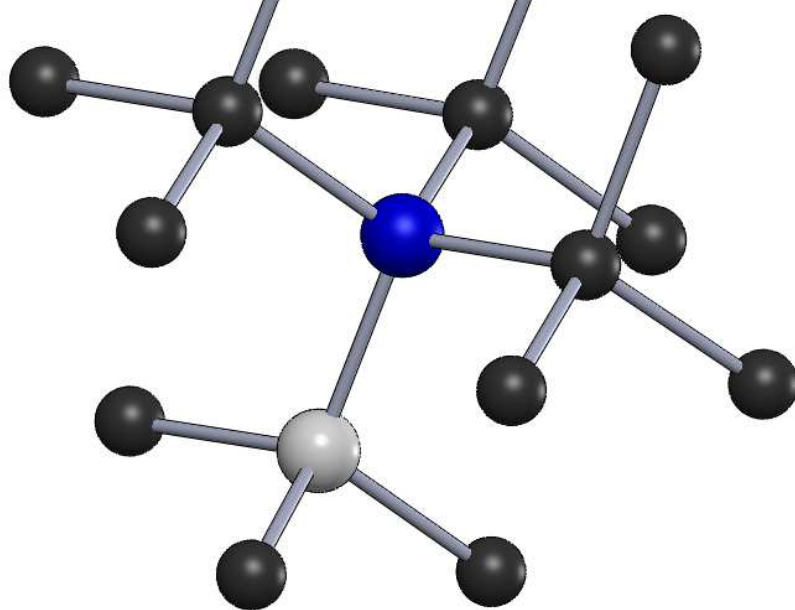
[36] Trusheim M E and Englund D 2016 *New Journal of Physics* **18** 123023 ISSN 1367-2630

- [37] Glenn D R, Fu R R, Kehayias P, Sage D L, Lima E A, Weiss B P and Walsworth R L 2017 *Geochemistry, Geophysics, Geosystems* **18** 3254–3267 ISSN 1525-2027
- [38] Rahn-Lee L, Byrne M E, Zhang M, Sage D L, Glenn D R, Milbourne T, Walsworth R L, Vali H and Komeili A 2015 *PLOS Genetics* **11** e1004811 ISSN 1553-7404
- [39] Eshelby J D 1954 *Journal of Applied Physics* **25** 255–261 ISSN 0021-8979
- [40] Ziegler J F, Ziegler M D and Biersack J P 2010 *Nuclear Instruments and Methods in Physics Research Section B: Beam Interactions with Materials and Atoms* **268** 1818–1823 ISSN 0168-583X
- [41] Zhang H, Arai K, Belthangady C, Jaskula J C and Walsworth R L 2017 *npj Quantum Information* **3** 1–8 ISSN 2056-6387
- [42] Hart C A, M S J, Turner M J, Scheidegger P J, Bauch E and Walsworth R L 2020 *in prep.*
- [43] Kucsko G, Maurer P C, Yao N Y, Kubo M, Noh H J, Lo P K, Park H and Lukin M D 2013 *Nature* **500** 54–58 ISSN 1476-4687
- [44] Neumann P, Jakobi I, Dolde F, Burk C, Reuter R, Waldherr G, Honert J, Wolf T, Brunner A, Shim J, Suter D, Sumiya H, Isoya J and Wrachtrup J 2013 *Nano Letters* **13** 2738–2742 ISSN 1530-6984
- [45] Toyli D M, Casas C F d l, Christle D J, Dobrovitski V V and Awschalom D D 2013 *Proceedings of the National Academy of Sciences* **110** 8417–8421 ISSN 0027-8424, 1091-6490
- [46] Chasles F, Dubertret B and Boccara A C 2007 *Optics Express* **15** 16130–16140 ISSN 1094-4087
- [47] Yang X, Tzeng Y K, Zhu Z, Huang Z, Chen X, Liu Y, Chang H C, Huang L, Li W D and Xi P 2014 *RSC Advances* **4** 11305–11310 ISSN 2046-2069
- [48] Keller P and Ahrens M 2015 *Neuron* **85** 462–483 ISSN 0896-6273
- [49] Horsley A, Appel P, Wolters J, Achard J, Tallaire A, Maletinsky P and Treutlein P 2018 *Physical Review Applied* **10** 044039
- [50] Pinto H, Jones R, Goss J P and Briddon P R 2011 *Journal of Physics: Conference Series* **281** 012023 ISSN 1742-6596
- [51] Marshall M C, Ku M J, Turner M J, Delegan N, Zhou T, Holt M V, Phillips D F and Walsworth R L 2020 *in prep.*
- [52] Grazioso F, Patton B R, Delaney P, Markham M L, Twitchen D J and Smith J M 2013 *Applied Physics Letters* **103** 101905 ISSN 0003-6951
- [53] Fu K M C, Santori C, Barclay P E, Rogers L J, Manson N B and Beausoleil R G 2009 *Physical Review Letters* **103** 256404
- [54] Bersin E, Walsh M, Mouradian S L, Trusheim M E, Schröder T and Englund D 2019 *npj Quantum Information* **5** 1–6 ISSN 2056-6387
- [55] Tamarat P, Gaebel T, Rabeau J, Khan M, Greentree A, Wilson H, Hollenberg L, Prawer S, Hemmer P, Jelezko F and Wrachtrup J 2006 *Physical Review Letters* **97** 083002
- [56] Geiselmann M, Juan M L, Renger J, Say J M, Brown L J, de Abajo F J G, Koppens F and Quidant R 2013 *Nature Nanotechnology* **8** 175–179 ISSN 1748-3395
- [57] Antonov D, Häußermann T, Aird A, Roth J, Trebin H R, Müller C, McGuinness L, Jelezko F, Yamamoto T, Isoya J, Pezzagna S, Meijer J and Wrachtrup J 2014 *Applied Physics Letters* **104** 012105 ISSN 0003-6951
- [58] Chakravarthi S, Moore C, Opsvig A, Pederson C, Hunt E, Ivanov A, Christen I, Dunham S and Fu K M C 2020 *Physical Review Materials* **4** 023402
- [59] Akselrod M S, Yoder R C and Akselrod G M 2006 *Radiation Protection Dosimetry* **119** 357–362 ISSN 0144-8420
- [60] Niklas M, Bartz J A, Akselrod M S, Abollahi A, Jäkel O and Greilich S 2013 *Physics in Medicine and Biology* **58** N251–N266 ISSN 0031-9155
- [61] Niklas M, Greilich S, Melzig C, Akselrod M S, Debus J, Jäkel O and Abdollahi A 2013 *Radiation Oncology* **8** 141 ISSN 1748-717X
- [62] Kouwenberg J J M, Wolterbeek H T, Denkova A G and Bos A J J 2018 *Radiation Oncology (London, England)* **13** ISSN 1748-717X URL

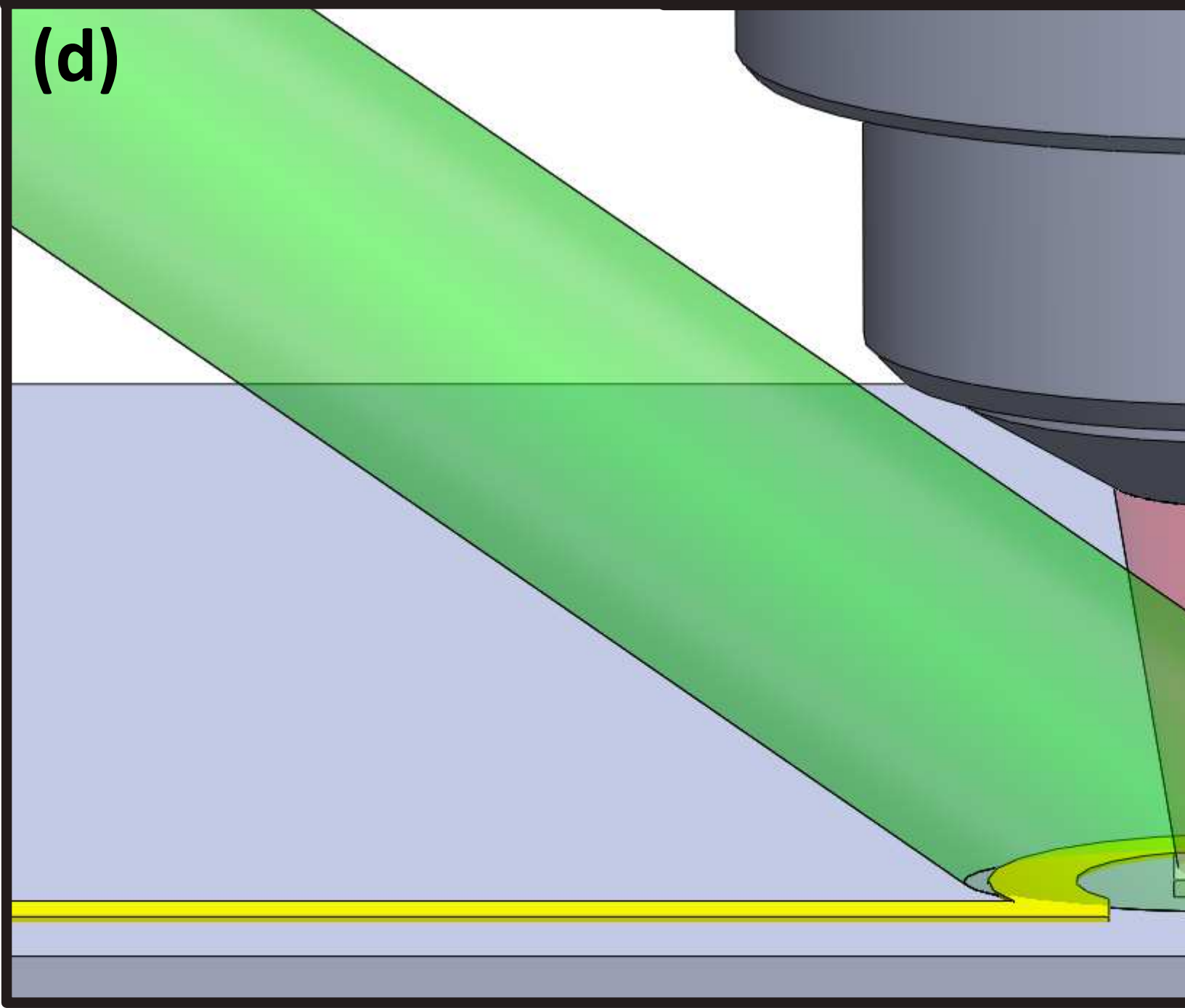
<https://www.ncbi.nlm.nih.gov/pmc/articles/PMC5992759/>

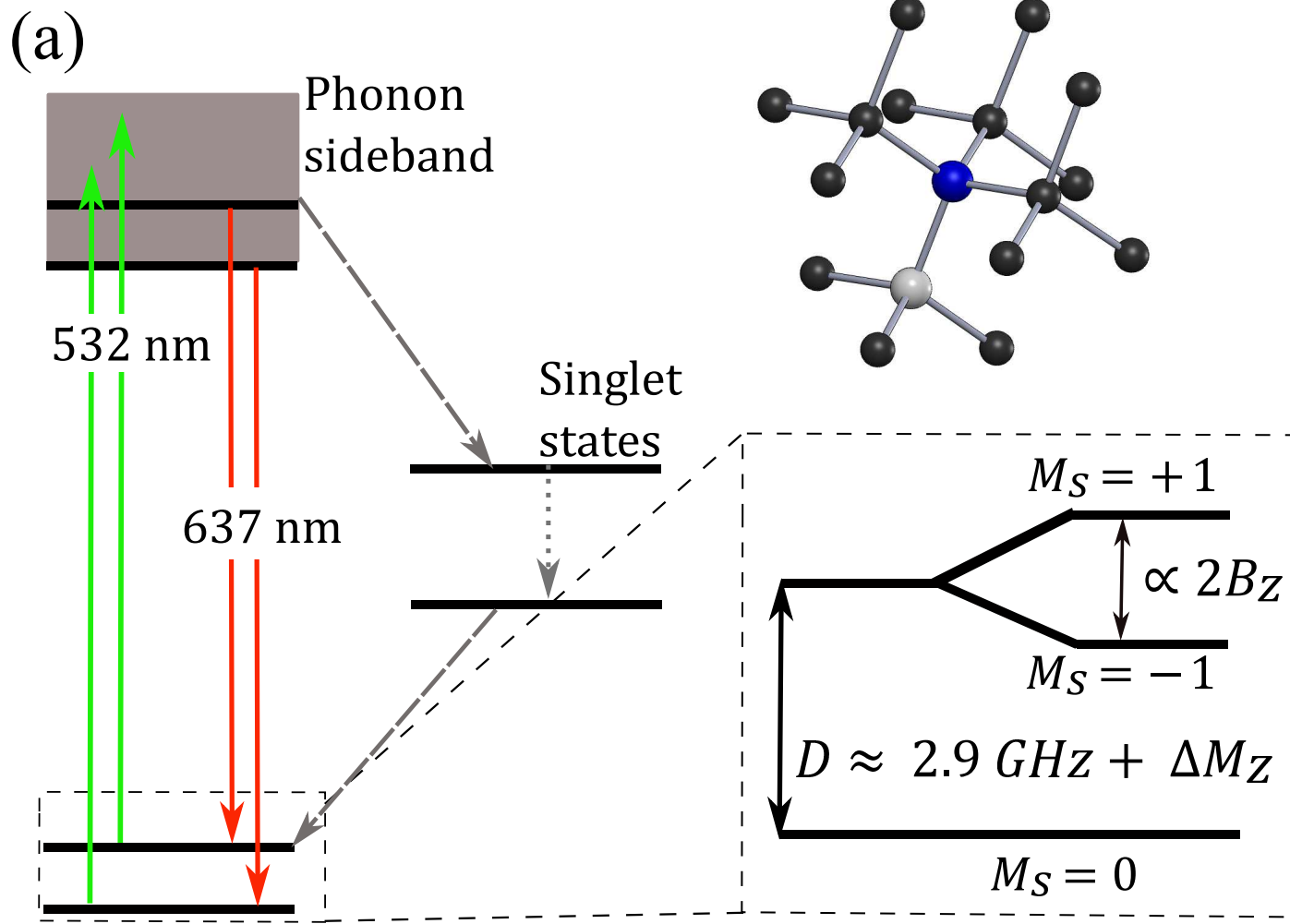
- [63] Bartz J A, Kodaira S, Kurano M, Yasuda N and Akselrod M S 2014 *Nuclear Instruments and Methods in Physics Research Section B: Beam Interactions with Materials and Atoms* **335** 24–30 ISSN 0168-583X
- [64] Fomenko V, Moreno B, Million M, Harrison J and Akselrod M 2018 *Radiation Protection Dosimetry* **180** 215–219 ISSN 0144-8420
- [65] Underwood T S A, Sung W, McFadden C H, McMahon S J, Hall D C, McNamara A L, Paganetti H, Sawakuchi G O and Schuemann J 2017 *Physics in Medicine and Biology* **62** 3237–3249 ISSN 0031-9155
- [66] Niklas M, Henrich M, Jäkel O, Engelhardt J, Abdollahi A and Greilich S 2017 *Physics in Medicine and Biology* N180–N190
- [67] Kouwenberg J J M, Kremers G J, Slotman J A, Wolterbeek H T, Houtsmuller A B, Denkova A G and Bos A J J 2018 *Journal of Microscopy* **270** 326–334 ISSN 1365-2818
- [68] Onoda S, Haruyama M, Teraji T, Isoya J, Kada W, Hanaizumi O and Ohshima T 2015 *physica status solidi (a)* **212** 2641–2644 ISSN 1862-6319
- [69] Onoda S, Tatsumi K, Haruyama M, Teraji T, Isoya J, Kada W, Ohshima T and Hanaizumi O 2017 *physica status solidi (a)* **214** 1700160 ISSN 1862-6319
- [70] Chen L, Miao X, Ma H, Guo L, Wang Z, Yang Z, Fang C and Jia X 2018 *CrystEngComm* **20** 7164–7169 ISSN 1466-8033
- [71] Farfurnik D, Alfasi N, Masis S, Kauffmann Y, Farchi E, Romach Y, Hovav Y, Buks E and Bar-Gill N 2017 *Applied Physics Letters* **111** 123101 ISSN 0003-6951
- [72] Deák P, Aradi B, Kaviani M, Frauenheim T and Gali A 2014 *Physical Review B* **89** 075203
- [73] Haque A and Sumaiya S 2017 *Journal of Manufacturing and Materials Processing* **1** 6
- [74] Wang Z H and Takahashi S 2013 *Physical Review B* **87** 115122
- [75] Rubinas c R, Vorobyov V V, Soshenko V V, Bolshedvorskii S V, Sorokin V N, Smolyaninov A N, Vins V G, Yelisseyev A P and Akimov A V 2018 *Journal of Physics Communications* **2** 115003 ISSN 2399-6528
- [76] Boretti A and Castelletto S 2016 *MethodsX* **3** 297–306 ISSN 2215-0161
- [77] Boretti A, Rosa L, Blackledge J and Castelletto S 2019 *Beilstein Journal of Nanotechnology* **10** 2128–2151 ISSN 2190-4286
- [78] Rittweger E, Han K Y, Irvine S E, Eggeling C and Hell S W 2009 *Nature Photonics* **3** 144–147 ISSN 1749-4893
- [79] Wildanger D, Patton B, Schill H, Marseglia L, Hadden J, Knauer S, Schönle A, Rarity J, O'Brien J, Hell S and Smith J 2012 *Advanced Materials* OP309–OP313
- [80] Arroyo-Camejo S, Adam M P, Besbes M, Hugonin J P, Jacques V, Greffet J J, Roch J F, Hell S W and Treussart F 2013 *ACS Nano* **7** 10912–10919 ISSN 1936-0851
- [81] Chen X, Zou C, Gong Z, Dong C, Guo G and Sun F 2015 *Light: Science & Applications* **4** e230–e230 ISSN 2047-7538
- [82] Chen X D, Li D F, Zheng Y, Li S, Du B, Dong Y, Dong C H, Guo G C and Sun F W 2019 *Physical Review Applied* **12** 044039
- [83] Maurer P, Maze J, Stanwix P, Jiang L, Gorshkov A, Zibrov A, Harke B, Hodges J, Zibrov A, Yacoby A, Twitchen D, Hell S, Walsworth R and Lukin M 2010 *Nature Physics* **6** 912–918 ISSN 1745-2481
- [84] Jaskula J C, Bauch E, Arroyo-Camejo S, Lukin M D, Hell S W, Trifonov A S and Walsworth R L 2017 *Optics Express* **25** 11048–11064 ISSN 1094-4087
- [85] Yang X, Xie H, Alonas E, Liu Y, Chen X, Santangelo P J, Ren Q, Xi P and Jin D 2016 *Light: Science & Applications* **5** e16134–e16134 ISSN 2047-7538
- [86] Han K Y, Willig K I, Rittweger E, Jelezko F, Eggeling C and Hell S W 2009 *Nano Letters* **9** 3323–3329 ISSN 1530-6984
- [87] Schmidt R, Wurm C A, Jakobs S, Engelhardt J, Egner A and Hell S W 2008 *Nature Methods* **5** 539–544 ISSN 1548-7105

- [88] Chen E H, Gaathon O, Trusheim M E and Englund D 2013 *Nano Letters* **13** 2073–2077 ISSN 1530-6984
- [89] Pfender M, Aslam N, Waldherr G, Neumann P and Wrachtrup J 2014 *Proceedings of the National Academy of Sciences* **111** 14669–14674 ISSN 0027-8424, 1091-6490
- [90] Zgadzai O, Shtirberg L, Artzi Y and Blank A 2017 *EPL (Europhysics Letters)* **117** 10001 ISSN 0295-5075
- [91] Bodenstedt S, Jakobi I, Michl J, Gerhardt I, Neumann P and Wrachtrup J 2018 *Nano Letters* **18** 5389–5395 ISSN 1530-6984
- [92] Arai K, Belthangady C, Zhang H, Bar-Gill N, DeVience S J, Cappellaro P, Yacoby A and Walsworth R L 2015 *Nature Nanotechnology* **10** 859–864 ISSN 1748-3395
- [93] Ziem F, Garsi M, Fedder H and Wrachtrup J 2019 *Scientific Reports* **9** 12166 ISSN 2045-2322
- [94] Haeberlé O, Ammar M, Furukawa H, Tenjimbayashi K and Török P 2003 *Optics Express* **11** 2964–2969 ISSN 1094-4087
- [95] Mimura H, Handa S, Kimura T, Yumoto H, Yamakawa D, Yokoyama H, Matsuyama S, Inagaki K, Yamamura K, Sano Y, Tamasaku K, Nishino Y, Yabashi M, Ishikawa T and Yamauchi K 2010 *Nature Physics* **6** 122–125 ISSN 1745-2481
- [96] Schülli T U and Leake S J 2018 *Current Opinion in Solid State and Materials Science* **22** 188–201 ISSN 1359-0286
- [97] Holt M, Harder R, Winarski R and Rose V 2013 *Annual Review of Materials Research* **43** 183–211
- [98] Winarski R, Holt M, Rose V, Fuesz P, Carbaugh D, Benson C, Shu D, Kline D, Stephenson G, McNulty I and Maser J 2012 *Journal of Synchrotron Radiation* **19** 1056–1060 ISSN 0909-0495
- [99] Nazaretski E, Yan H, Lauer K, Bouet N, Huang X, Xu W, Zhou J, Shu D, Hwu Y and Chu Y S 2017 *Journal of Synchrotron Radiation* **24** 1113–1119 ISSN 1600-5775
- [100] Johansson U, Carbone D, Kalbfleisch S, Bjorling A, Rodriguez-Frenandez A, Stankevic T, Liebi M, Bring B, Mikkelsen A and Vogt U 2018 *Microscopy and Microanalysis* **24** 250–251 ISSN 1431-9276, 1435-8115
- [101] Qazilbash M, Tripathi A, Schafgans A, Kim B J, Kim H T, Cai Z, Holt M, Maser J, Keilmann F, Shpyrko O and Basov D 2011 *Physical Review B* **83** 165108
- [102] Hruszkewycz S O, Highland M J, Holt M V, Kim D, Folkman C M, Thompson C, Tripathi A, Stephenson G B, Hong S and Fuoss P H 2013 *Physical Review Letters* **110** 177601
- [103] Hruszkewycz S O, Holt M V, Maser J, Murray C E, Highland M J, Folkman C M and Fuoss P H 2014 *Philosophical transactions. Series A, Mathematical, physical, and engineering sciences* **372** ISSN 1364-503X URL <https://www.ncbi.nlm.nih.gov/pmc/articles/PMC3900036/>
- [104] Hruszkewycz S O, Allain M, Holt M V, Murray C E, Holt J R, Fuoss P H and Chamard V 2017 *Nature Materials* **16** 244–251 ISSN 1476-4660
- [105] Hill M, Calvo-Almazan I, Allain M, Holt M, Ulvestad A, Treu J, Koblmüller G, Huang C, Huang X, Yan H, Nazaretski E, Chu Y, Stephenson G, Chamard V, Lauhon L and Hruszkewycz S 2018 *Nano Letters* **18** 811–819 ISSN 1530-6984
- [106] Evans P G, Savage D E, Prance J R, Simmons C B, Lagally M G, Coppersmith S N, Eriksson M A and Schülli T U 2012 *Advanced Materials* **24** 5217–5221 ISSN 1521-4095



(d)

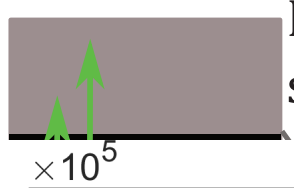




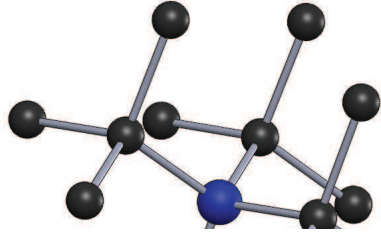
(b)

Fluorescence

(a)



Phonon
sideband



(b)

Count

